

On MSSM charged Higgs-boson production in association with an electroweak W boson at electron–positron colliders

Oliver Brein

Institute for Particle Physics Phenomenology,
University of Durham, DH1 3LE, Durham, United Kingdom

Thomas Hahn

Max-Planck-Institut für Physik
D-80805 München, Germany

Abstract

We present a calculation of the cross section for the process $e^+e^- \rightarrow W^\pm H^\mp$ in the Minimal Supersymmetric Standard Model (MSSM) and the Two Higgs Doublet Model (THDM). We study the basic features of the MSSM prediction for some distinctive parameter scenarios. We find large effects from virtual squarks for scenarios with large mixing in the stop sector which can lead to a cross section vastly different from a THDM with identical Higgs-sector parameters. We investigate this interesting behaviour in more detail by thoroughly scanning the MSSM parameter space for regions of large cross section. For a charged Higgs boson too heavy to be pair-produced at such a machine, it turns out that a large MSSM cross section with a good chance of observation is linked to a squark mass scale below 600 GeV and a considerable amount of mixing in either the stop and sbottom sector.

1 Introduction

The discovery potential of the CERN Large Hadron Collider (LHC) should be sufficient to resolve the issue of the existence of a neutral Higgs boson [1]. An electron–positron collider would, however, serve as an ideal tool to measure the properties of neutral Higgs bosons very precisely [2]. To discover a charged Higgs boson, H^\pm , on the other hand, is much harder at the LHC [1, 3], especially if the H^\pm is substantially heavier than the top quark. The reason for this is the dominant decay of the H^\pm bosons into heavy quarks ($t\bar{b}$ or $\bar{t}b$) which leads to hadronic signatures that are hard to distinguish from QCD background events and which forces one either to rely on the less probable decay $H^\pm \rightarrow \tau\nu$ or to accumulate a lot of statistics during several years of running at high luminosity in order to claim discovery. Actually, the strong dependence of the production cross sections on the ratio of vacuum expectation values in the Higgs sector, $v_2/v_1 = \tan\beta$, makes it almost impossible to discover the charged Higgs boson at the LHC in a wedge-shaped region of intermediate $\tan\beta$ -values in the $\tan\beta$ – m_{H^\pm} plane if it is heavier than the top-quark [1, 3]. This non-discovery range includes $4 \lesssim \tan\beta \lesssim 12$ at $m_{H^\pm} = 250$ GeV and widens continuously to e.g. $2 \lesssim \tan\beta \lesssim 40$ at $m_{H^\pm} = 650$ GeV [3].

At an e^+e^- collider with a centre-of-mass energy \sqrt{s} , the main production process for charged Higgs bosons is pair production ($e^+e^- \rightarrow H^+H^-$) which is mediated mainly via photon- and Z -exchange in the s-channel. The pair-production cross section is almost independent of $\tan\beta$ and, owing to the colourless initial state, Higgs-boson signatures from decays into heavy quarks are not obscured by enormous amounts of QCD background events, like at the LHC. Therefore, detection of charged Higgs bosons via pair production should be possible in the whole m_{H^\pm} – $\tan\beta$ plane up to a mass limit somewhat below $\sqrt{s}/2$. If the collider energy is not sufficient for pair production (i.e. $\sqrt{s} < 2m_{H^\pm}$), the only way to extend the search for the charged Higgs boson to higher masses is to try to observe its single production in association with lighter particles. The most relevant processes which have been studied in the literature are the tree-level processes $e^+e^- \rightarrow H^\pm\tau\nu$ [4, 5] and $e^+e^- \rightarrow H^\pm tb$ [6, 5], and the loop-induced processes $e^+e^- \rightarrow H^\pm e\nu$ [7, 8, 5] and $e^+e^- \rightarrow W^\pm H^\mp$ [9, 10, 11, 12, 13, 5]. Most of the studies are done in the framework of a Two Higgs Doublet Model (THDM) with parameters fixed at MSSM values, except for Refs. [11, 12] which study $W^\pm H^\mp$ production in the general THDM, Refs. [9, 13] which study the same process in the full MSSM, and Ref. [8] which includes virtual sfermion contributions for the cross section prediction of the $H^\pm e\nu_e$ final state.

If the collider energy does not allow for pair production and $\sqrt{s} > m_W + m_{H^\pm}$, the $W^\pm H^\mp$ production process can become the dominant source of charged Higgs bosons, depending on $\tan\beta$. In this case, as the process is loop-induced, the signal rate is much smaller than the typical pair-production rate. Even if H^+H^- production is the main production process at an e^+e^- collider, it would still be very rewarding to measure the $W^\pm H^\mp$ production cross section as well. While the H^+H^- cross section is determined at tree-level by the gauge couplings to photon and Z -boson, the $W^\pm H^\mp$ cross section is loop-induced and thus depends already at leading order on the virtual particles in the loops. Therefore, with a cross section measurement of the latter process one would have access

to information about the underlying model.

This paper presents a calculation of the MSSM prediction for the process $e^+e^- \rightarrow W^+H^-$. By the time this work was finalized, another calculation of the same prediction appeared [9]. We carried out a detailed comparison [14] of our results with those of Ref. [9] which lead to agreement¹. In the framework of the Two Higgs Doublet Model (THDM), the cross section prediction for $e^+e^- \rightarrow W^+H^-$ is well-known [10, 11, 12] and we could reproduce the results of Ref. [12] in particular.

In Section 2 we present the process $e^+e^- \rightarrow W^+H^-$ with the contributing Feynman diagrams in the MSSM and some details about our calculation. Section 3 presents our numerical results in two stages. In stage one, we examine the basic features of the $W^\pm H^\mp$ cross section for a 500 GeV and 1 TeV e^+e^- collider for two distinct MSSM parameter scenarios and compare the results also to predictions of a THDM with the same Higgs sector parameters. This enables us to exemplify the range of influence of virtual superpartners on the cross section. The effect of polarized electron and positron beams on the cross section is discussed briefly followed by a demonstration of the decoupling of superpartners with increasing supersymmetry-breaking scale. In stage two, we present results of a thorough scan of the MSSM parameter space for regions of large, possibly observable, cross section and try to understand for which parameter scenarios they arise. Section 4 contains our conclusions. Some results of this calculation were already reported in [13].

2 $e^+e^- \rightarrow W^+H^-$ in the MSSM

2.1 Kinematics

We study the reaction

$$e^+(\bar{k}, \bar{\sigma}) + e^-(k, \sigma) \rightarrow W^+(p, \lambda) + H^-(\bar{p}),$$

where k and \bar{k} denote the momenta of the initial-state electron and positron, p and \bar{p} the momenta of the final-state gauge boson W^+ and Higgs boson H^- . Additionally, the electron, positron, and W -boson are characterized by their spin polarization $\sigma, \bar{\sigma} (= \pm \frac{1}{2})$ and $\lambda (= 0, \pm 1)$. Neglecting the electron mass, the kinematical invariants $s = (k + \bar{k})^2$, $t = (k - p)^2$ and $u = (k - \bar{p})^2$ fulfil the relation

$$s + t + u = m_W^2 + m_{H^\pm}^2. \quad (1)$$

We assume unpolarized electron and positron beams. Thus, the differential cross section summed over spin polarizations of the final-state W -boson reads

$$\frac{d\sigma}{dt} = \frac{1}{16\pi s^2} \sum_{\lambda=0,\pm 1} \frac{1}{4} \sum_{\sigma,\bar{\sigma}=\pm \frac{1}{2}} |\mathcal{M}_{\sigma\bar{\sigma}\lambda}|^2 \quad (2)$$

¹ As a result, the formulae in [9] are now checked by an independent calculation. According to [14] the results agree, if in Eq. (C14) of Ref. [9] the tensor coefficient D_{23} in the coefficient of $\mathcal{A}_6 g_R^W g_H^L$ is replaced by $2D_{23}$.

with the helicity amplitudes $\mathcal{M}_{\sigma\bar{\sigma}\lambda}$ of the process. The total cross section is evaluated by numerical integration over the kinematically allowed t -range:

$$\sigma_{e^+e^- \rightarrow W^+H^-}(s) = \int_{t_{\min}(s)}^{t_{\max}(s)} dt \frac{d\sigma}{dt}(s, t). \quad (3)$$

2.2 Feynman graphs

In the MSSM and THDM all leptons couple gauge-invariantly to one of the two Higgs doublets and therefore also to the physical Higgs bosons. Thus, there is a non-vanishing tree-level amplitude for the process under study. The Feynman graphs on tree-level consist of three graphs with s -channel exchange of neutral Higgs bosons (h^0, H^0, A^0) and one with a t -channel exchange of a neutrino. The Yukawa couplings which appear in all tree-level graphs are $\propto m_e/m_W \approx 6 \cdot 10^{-6}$ and suppress the tree-level contribution strongly. The tree-level amplitude can thus safely be neglected and consequently there are no photon bremsstrahlung corrections at leading order.

In our calculation we take into account all one-loop contributions to the amplitude which do not vanish in the limit $m_e = 0$. For this reason, Feynman graphs with insertion of a s -channel Z - A mixing self-energy, or a t -channel neutrino self-energy, or radiative corrections to $e^+e^- \{h^0, H^0, A^0\}$ Yukawa couplings or to the $e^\pm \nu_e H^\mp$ Yukawa coupling need not be considered. There remain Feynman graphs with insertions of a W^- - H^- or G^- - H^- mixing self-energy at the external leg of the outgoing charged Higgs boson (see Fig. 1), graphs containing the loop-induced $\gamma W^+ H^-$ and $Z W^+ H^-$ vertices² and box-type graphs (see Fig. 2 and 3). The amplitude divides into Feynman graphs which contain either solely THDM particles (Fig. 1b,c upper lines and Fig. 2), or solely superpartners (Fig. 1b,c lower lines and Fig. 3) in the loop.

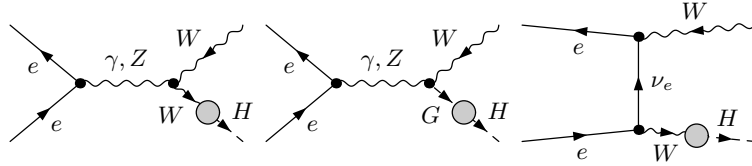
2.3 Calculation

Although the tree-level contribution vanishes in the the limit of vanishing electron mass, which we consider, the need for renormalization arises at one-loop. There are divergent vector-scalar and scalar-scalar mixing propagators (Fig. 1) and vertex-type graphs (Fig. 2 and 3)³. We use the on-shell renormalization scheme of Ref. [16], the application of which to W^\pm - H^\mp self-energies is discussed in detail in Ref. [17]. In the MSSM no new types of divergent vertex functions occur. Merely, additional loop contributions with virtual superpartners add to the existing types of vertex functions. Therefore, we can take over the renormalization conditions from Ref. [12] directly, which are briefly summarized in the following.

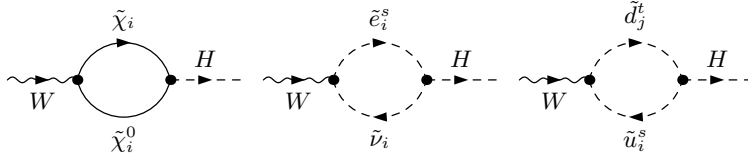
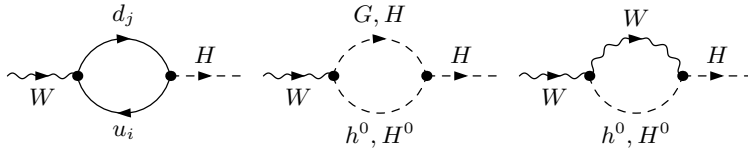
In order to generate the counter-terms, which are needed to renormalize the amplitude under study, it is sufficient to introduce field renormalization constants for the MSSM

²Note that there is no tree-level $ZW^\pm H^\mp$ coupling in the MSSM or THDM [15].

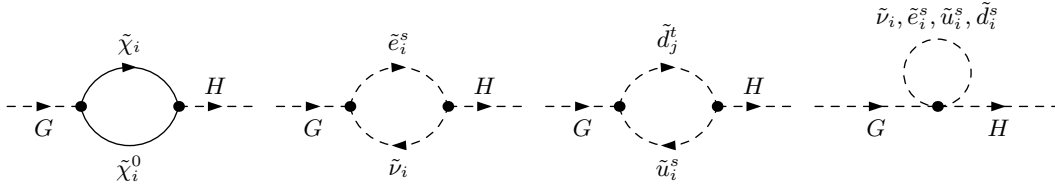
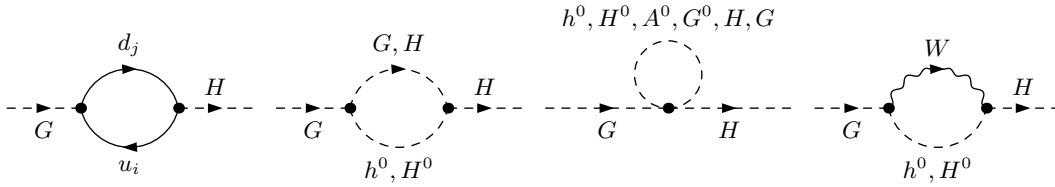
³In principle, also divergent tadpole insertions appear which we do not display, because we will choose a renormalization condition such that those contributions vanish (see Eqs. (9) and (10)).



(a) graphs with self-energy insertions



(b) W^+H^- self-energy



(c) G^+H^- self-energy

Figure 1: Feynman graphs for the process $e^+e^- \rightarrow W^+H^-$ with self-energy insertions. Each combination of particle labels corresponds to a separate Feynman graph.

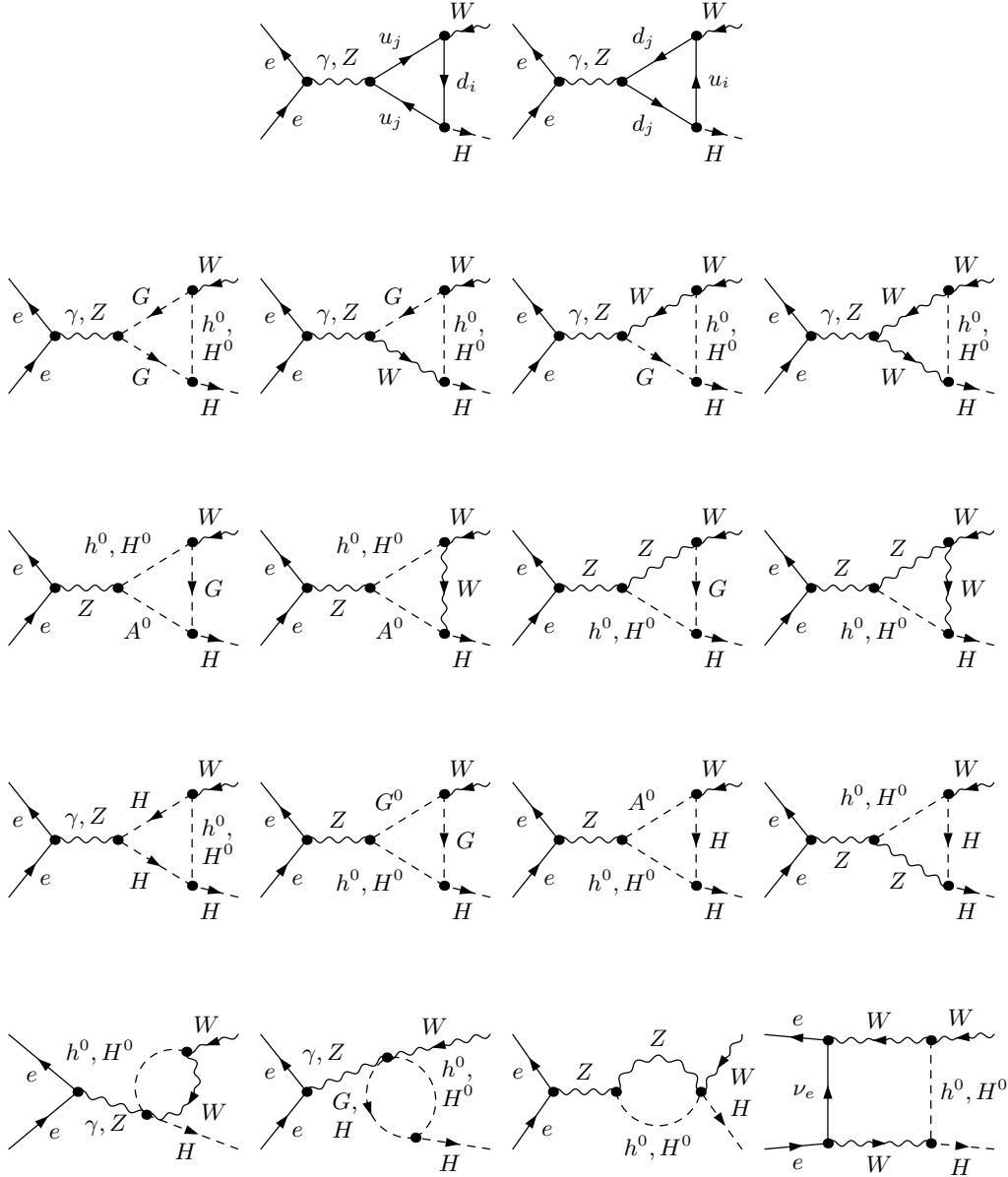


Figure 2: The THDM subset of Feynman graphs of vertex and box type for the process $e^+e^- \rightarrow W^+H^-$. Each combination of particle labels corresponds to a separate Feynman graph.

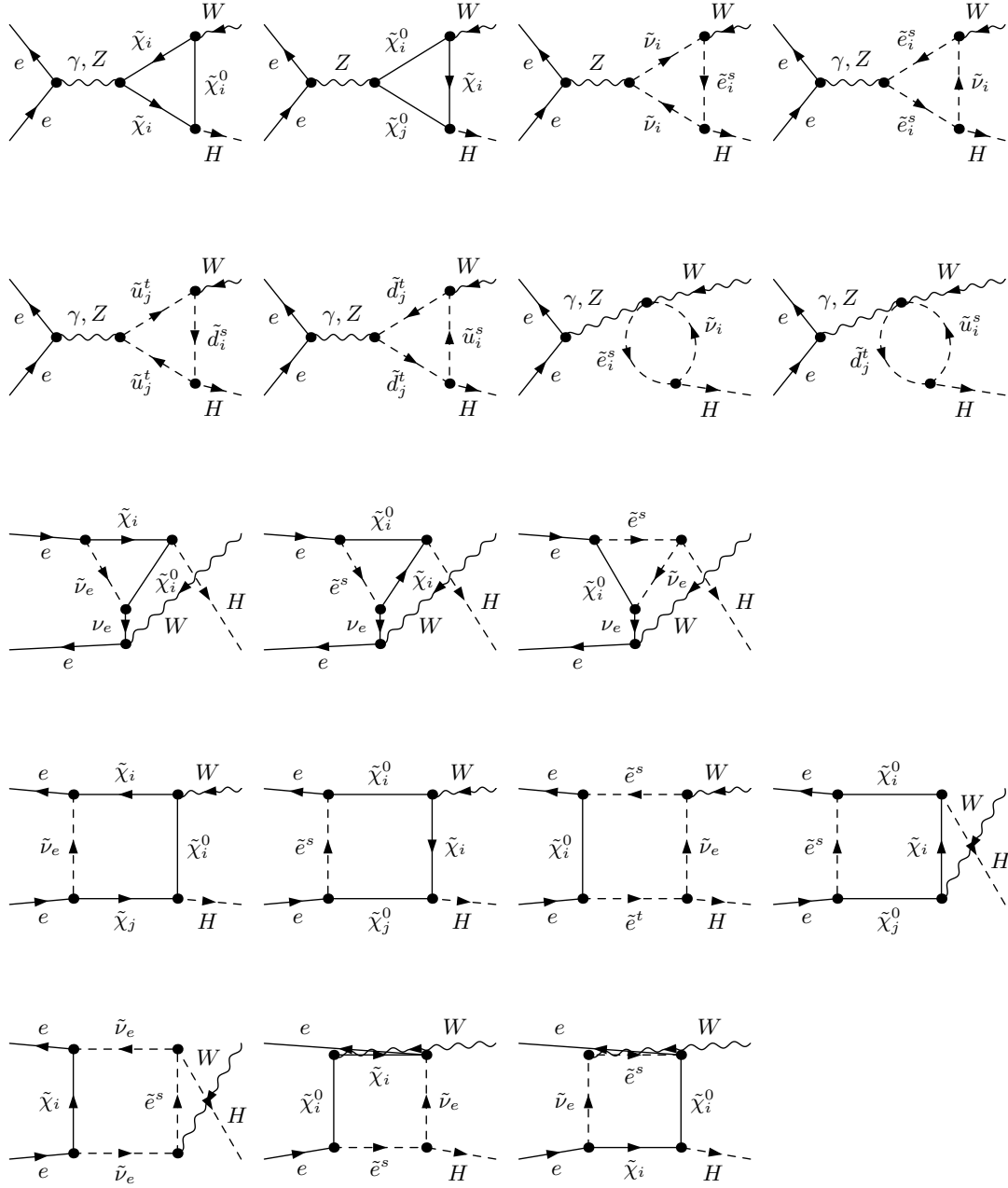


Figure 3: The superpartner-loop subset of vertex and box type for the process $e^+e^- \rightarrow W^+H^-$. Each combination of particle labels corresponds to a separate Feynman graph.

Higgs doublets H_1, H_2 and renormalization constants for their vacuum expectation values v_1, v_2 :

$$H_i \rightarrow \sqrt{Z_{H_i}} H_i, \quad v_i \rightarrow \sqrt{Z_{H_i}} (v_i - \delta v_i), \quad i = 1, 2. \quad (4)$$

Expanding the renormalization constants in the MSSM Lagrangian to one-loop order, $Z_{H_i} = 1 + \delta Z_{H_i}^{(1)}$ and $\delta v_i = \delta v_i^{(1)}$, generates the counter-term interactions needed and the corresponding Feynman rules:

$$\Gamma_{\text{CT}}[H^\mp W^\pm(k^\mu)] = i \frac{k^\mu}{m_W} m_W^2 \delta Z_{HW}, \quad (5)$$

$$\Gamma_{\text{CT}}[\gamma_\mu W_\nu^\pm H^\mp] = -i e m_W g_{\mu\nu} \delta Z_{HW}, \quad (6)$$

$$\Gamma_{\text{CT}}[Z_\mu W_\nu^\pm H^\mp] = i e m_W \frac{s_w}{c_w} g_{\mu\nu} \delta Z_{HW} \quad (7)$$

with

$$\delta Z_{HW} = \sin \beta \cos \beta \left(\frac{\delta v_1}{v_1} - \frac{\delta v_2}{v_2} + \frac{\delta Z_{H_2} - \delta Z_{H_1}}{2} \right), \quad (8)$$

where Z, W^\pm and γ denote the electroweak gauge bosons and the photon, and k^μ the momentum of the W^\pm boson, chosen as incoming. In the on-shell scheme the following renormalization conditions are posed:

- Renormalized tadpole graphs vanish, i.e.

$$\hat{t}_{h^0} = t_{h^0} + \delta t_{h^0} = 0, \quad (9)$$

$$\hat{t}_{H^0} = t_{H^0} + \delta t_{H^0} = 0. \quad (10)$$

This guarantees that the parameters v_1, v_2 in the renormalized Lagrangian describe the minimum of the Higgs potential at one-loop order.

- Real charged Higgs bosons H^\pm do not mix with longitudinally polarized W^\pm bosons, i.e. the real part of the renormalized H^\pm - W^\mp mixing self-energy⁴,

$$\hat{\Sigma}_{HW}(k^2) = \Sigma_{HW}(k^2) - m_W^2 \delta Z_{HW}, \quad (11)$$

vanishes if the momentum k of H^\pm is on mass-shell:

$$\text{Re } \hat{\Sigma}_{HW}(k^2) \Big|_{k^2=m_{H^\pm}^2} = 0. \quad (12)$$

The condition (12) fixes the renormalization constant δZ_{HW} :

$$\delta Z_{HW} = \frac{1}{m_W^2} \text{Re } \Sigma_{HW}(m_{H^\pm}^2). \quad (13)$$

⁴ The renormalized H^\pm - W^\mp mixing self-energy is defined as the coefficient of $-i \frac{k^\mu}{m_W}$ of the amputated renormalized H^\pm - W^\mp propagator.

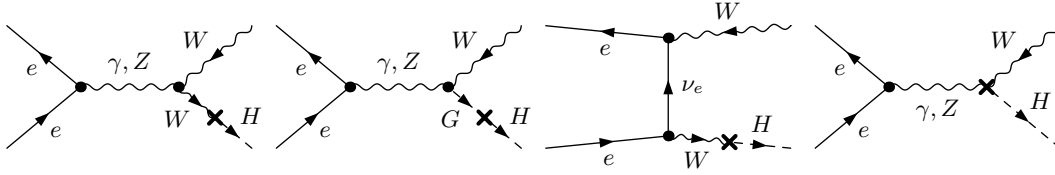


Figure 4: Counter-term diagrams for $e^+e^- \rightarrow W^+H^-$.

Because of the BRS symmetry of the renormalized Lagrangian the renormalization of the divergent H^\pm - G^\mp mixing self-energy is connected with the H^\pm - W^\mp mixing self-energy through a Slavnov–Taylor identity [17]:

$$k^2 \hat{\Sigma}_{HW}(k^2) - m_W^2 \hat{\Sigma}_{HG}(k^2) = 0. \quad (14)$$

As a consequence, the real part of the renormalized H^\pm - G^\mp mixing self-energy,

$$\hat{\Sigma}_{HG}(k^2) = \Sigma_{HG}(k^2) - k^2 \delta Z_{HG}, \quad (15)$$

also vanishes for $k^2 = m_{H^\pm}^2$:

$$\text{Re } \hat{\Sigma}_{HG}(k^2) \Big|_{k^2=m_{H^\pm}^2} = 0. \quad (16)$$

The Feynman rule for the corresponding counter-term interaction thus reads:

$$\Gamma_{\text{CT}}[H^\mp G^\pm(k)] = ik^2 \delta Z_{HG} \quad (17)$$

with $\delta Z_{HG} = -\text{Re } \Sigma_{HG}(m_{H^\pm}^2)/m_{H^\pm}^2$.

The calculation of the amplitude has been performed in 't Hooft–Feynman gauge using Constrained Differential Renormalization [18] with the help of the computer programs FeynArts and FormCalc [19]. To that end, the counter-term definitions and Feynman rules of counter-term interactions which were needed were added to the MSSM model file for FeynArts.

3 Results

Our presentation of results is meant to be exemplary. Given the possible time-line for the realization of a high-energy e^+e^- collider like the International Linear Collider (ILC) and given that it is not yet known what the LHC will reveal about this new energy frontier, there is no point in attempting a comprehensive presentation. The predictions for $W^\pm H^\mp$ production in the framework of the general THDM are well known [10, 11, 12]. Our concern is to demonstrate possible distinctive differences between the MSSM and the THDM. To that end, we compare the prediction of our complete one-loop calculation in the MSSM with the THDM prediction with the Higgs-sector parameters restricted to MSSM values (sTHDM). The latter model corresponds to the MSSM with decoupled superpartners. Thus, one achieves insight in the contribution of superpartner loop graphs to the cross section.

3.1 MSSM parameter scenarios

In order to demonstrate possible differences between the sTHDM and the full MSSM, we are interested in scenarios which potentially show large effects from virtual superpartners. Hence, the MSSM parameter scenarios for which we present numerical results have a rather low squark-mass scale. In the MSSM, large mixing in the stop sector is known to induce large radiative corrections in the Higgs sector. Therefore, we investigate two types of scenarios, one with large mixing in the stop sector and the other one with no mixing.

In order to specify the relevant MSSM parameters, let us recall the stop mass matrix. For real values of the supersymmetric Higgsino mass parameter μ and the soft-breaking parameter A_t the stop mass matrix reads in the L–R basis

$$M_{\tilde{t}}^2 = \begin{pmatrix} M_{\tilde{Q}}^2 + m_t^2 + m_Z^2(\frac{1}{2} - Q_t s_w^2) \cos 2\beta & m_t X_t \\ m_t X_t & M_{\tilde{U}}^2 + m_t^2 + m_Z^2 Q_t s_w^2 \cos 2\beta \end{pmatrix} \quad (18)$$

where $X_t = A_t - \mu \cot \beta$, $Q_t = 2/3$, and $s_w = \sin \theta_w$. $M_{\tilde{Q}}$ and $M_{\tilde{U}}$ are the soft-breaking masses for squark isospin-doublets and -singlets respectively. The two MSSM parameter scenarios are specified as follows:

Large-stop-mixing scenario: We set all sfermion mass parameters ($M_{\tilde{Q}}, M_{\tilde{U}}, M_{\tilde{D}}, M_{\tilde{L}}, M_{\tilde{E}}$) equal to one common sfermion mass scale $M_{\tilde{f}} = 350$ GeV, the stop mixing parameter $X_t = -806$ GeV, $\mu = 300$ GeV, the gaugino mass parameters $M_2 = 1000$ GeV and $M_1 = (5s_w^2/3c_w^2)M_2 = 476.26$ GeV (GUT relation).

The main features of this scenario are:

- The mass of the light stop is of order 100 GeV and there is a large mass splitting between the two stop mass eigenstates.
- The stop mixing angle is approximately 45° . Thus, maximal mixing occurs, i.e. all entries in the stop mixing matrix have approximately the same magnitude.
- The mass of the lightest MSSM Higgs boson m_h is almost maximal with respect to X_t (because $|X_t| \approx 2M_{\tilde{f}}$ [20]), e.g. for $m_{H^\pm} = 350$ GeV and $\tan \beta = 30$ we have $m_h = 120.06$ GeV.
- This scenario allows for the production of stop pairs at the energy scales considered in the following sections and the decay of the charged Higgs into stop and sbottom will be kinematically allowed for $m_{H^\pm} \gtrsim 450$ GeV.

No-stop-mixing scenario: Here, we choose the same values of the MSSM parameters as above, except for X_t which is set to zero.

The main features of this scenario are:

- Both stops have masses around 400 GeV and all other sfermions have masses around 350 GeV.

- The stop mixing angle is zero. Thus, no mixing occurs, i.e. the L–R basis for stops coincides with the mass basis.
- The mass of the lightest MSSM Higgs boson is rather low, e.g. $m_h = 103.02$ GeV for $m_{H^\pm} = 350$ GeV and $\tan\beta = 30$.

For the values of m_{H^\pm} and $\tan\beta$ chosen for our discussion, both scenarios respect all superpartner mass bounds from direct search results and fulfil indirect constraints on the parameters coming from requiring vacuum stability and from experimental bounds on the electroweak precision observables. Also the lower bound on the lightest neutral MSSM Higgs boson is respected by both scenarios, except for the case $\tan\beta = 3$ in the no-mixing scenario. Yet, for the sake of comparison, we also show this case among our numerical results.

3.2 Cross-section for the parameter scenarios

There are two major motivations for studying the MSSM prediction for $e^+e^- \rightarrow W^\pm H^\mp$ cross sections at a future ILC. Firstly, it is important to know the expected event rates at the ILC either to confirm the discovery of charged Higgs bosons at the LHC or to assess the H^\pm discovery potential of the ILC beyond the pair-production limit of $\sqrt{s}/2$. Secondly, the observation of this process provides the opportunity to glean some information about the underlying model because of its potential sensitivity to virtual superpartners.

We present results for two collider energies, $\sqrt{s} = 500$ GeV and 1000 GeV. For each energy we show results for the the large-stop-mixing and no-stop-mixing scenario for different $\tan\beta$ -values in and around the “wedge region” and for charged Higgs bosons masses below, above and right at the pair production limit of 250 and 500 GeV, respectively.

3.2.1 Large-stop-mixing scenario

In Figs. 5a and 6a the $e^+e^- \rightarrow W^\pm H^\mp$ cross sections for a collider energy of 500 GeV are displayed for the full MSSM and the corresponding sTHDM. Fig. 5a shows the m_{H^\pm} -dependence for $\tan\beta = 3, 15,$ and 30. The spike in all predictions for $m_{H^\pm} \equiv \sqrt{p^2} \approx 180$ GeV $\approx m_t + m_b$ is due to a threshold effect in the vertex graphs with virtual top- and bottom-quarks (see Fig. 2). Similar spikes appear in the full MSSM prediction in places where m_{H^\pm} equals $m_{\tilde{t}_i} + m_{\tilde{b}_j}$ ($i, j = 1, 2$) and are due to threshold effects in the Feynman graphs with virtual stops and sbottoms, e.g. for $\tan\beta = 30$ where $m_{H^\pm} \approx 390$ GeV $\approx m_{\tilde{t}_1} + m_{\tilde{b}_1}$. Fig. 6a shows the $\tan\beta$ -dependence for $m_{H^\pm} = 190$ GeV, 250 GeV, and 350 GeV. The MSSM cross section is generally about two orders of magnitude larger than the sTHDM in the large-stop-mixing case for large values of $\tan\beta$.

For $\sqrt{s} = 1000$ GeV Figs. 5b and 6b reveal the same general behaviour. Yet, due to the higher collider energy, more stop–sbottom thresholds are within the accessible mass range for the charged Higgs boson.

The enhancement with respect to the sTHDM case is due to the threshold effects combined with enhanced couplings of the charged Higgs boson to third-generation squarks.

In the large-stop-mixing scenario, the Feynman graphs with virtual squarks of the third generation comprise the dominant contribution to the cross section if $\tan \beta$ is not too small. In this scenario each entry of the rotation matrix which transforms the stop fields into the mass eigenbasis is of similar magnitude. Thus, all potentially large terms in the couplings of third-generation squarks to Higgs bosons⁵ are weighted by a factor of order 1, especially the term proportional to $m_t \mu$.

3.2.2 No-stop-mixing scenario

Figs. 5c and 6c show the predicted cross section for a 500 GeV collider in this scenario. Superpartner effects are small in this case and the MSSM as well as the sTHDM predict almost the same cross section. Without mixing in the stop sector the two factors which caused the large enhancement in the large-mixing case are absent. Firstly, there are no enhancement effects by thresholds in stop–sbottom loops. Secondly, the mixing angle in the stop sector is exactly zero which leads to the absence of terms proportional to $m_t \mu$ in the $\tilde{t}_1 \tilde{b}_i H^\pm$ -couplings.

For $\sqrt{s} = 1000$ GeV the situation changes (see Figs. 5d and 6d). The maximally accessible charged-Higgs-boson mass is higher than all thresholds in stop–sbottom loop graphs ($730 \text{ GeV} < m_{\tilde{t}_i} + m_{\tilde{b}_j} < 760 \text{ GeV}$). Again, there are threshold enhancements of the MSSM prediction with respect to the sTHDM of up to one order of magnitude for large $\tan \beta$.

3.2.3 Effect of polarized electrons and positrons

The cross section of $e^+ e^- \rightarrow W^\pm H^\mp$ depends strongly on the polarization of the incoming electrons and positrons. Specifically, the cross section varies roughly by one order of magnitude between the optimal situation where all electrons have helicity -1 and all positrons have helicity $+1$, i.e. $P(e^-) = -1$ and $P(e^+) = +1$, and the opposite situation where $P(e^-) = +1$ and $P(e^+) = -1$.

In order to illustrate the effect of polarized beams at a future LC, we include in Figs. 5a to 5d the cross section prediction for the optimal polarization for $\tan \beta = 15$. Likewise, we include in Figs. 6a to 6d the cross section prediction for the optimal polarization for $m_{H^\pm} = \sqrt{s}/2$. Optimal polarization leads to an increase in cross section varying between a factor of 2 up to 3.8 depending on m_{H^\pm} and $\tan \beta$ for both collider energies.

3.2.4 Decoupling of superpartners

We set all soft-breaking parameters which appear in our expression for the MSSM cross section equal to a single supersymmetry breaking scale \widetilde{M} ,

$$\widetilde{M} = M_{\tilde{f}} = A_b = A_t = M_1 = M_2 = \mu, \quad (19)$$

⁵A full list of the relevant couplings in our notation can be found in [21]

and study the behaviour of the MSSM cross section with rising \widetilde{M} compared to the sTHDM prediction. This will allow us to demonstrate the decoupling of the virtual superpartner contributions to the cross section.

Fig. 7a shows results for a 500 GeV collider and $m_{H^\pm} = 190, 250,$ and 350 GeV with \widetilde{M} varied between 350 and 2000 GeV. The MSSM results drop significantly once all superpartners get heavy enough for threshold effects to disappear. A similar behaviour is shown in Fig. 7b for a 1000 GeV collider and $m_{H^\pm} = 350, 500,$ and 650 GeV where \widetilde{M} is varied up to 4TeV. Notably, even at a soft-breaking scale of 1TeV, the MSSM surpasses the sTHDM prediction by a factor of 1.4, 1.7, and 2.2 for these three mass values, respectively.

3.3 Parameter scan

We demonstrated the possibility of strong enhancement of the MSSM cross section prediction by virtual superpartner effects for the large-stop-mixing scenario. This might predict $W^\pm H^\mp$ production to be observable in such MSSM scenarios unlike in the corresponding sTHDM scenario. We investigate this possible behaviour more systematically by scanning over the relevant MSSM parameter space.

The detectors at the LHC will be capable of finding an MSSM charged Higgs boson only in certain regions in the m_{A^0} - $\tan\beta$ plane. Likewise, the ILC can detect charged Higgs bosons easily only if pair production is kinematically possible. Thus, as far as $W^\pm H^\mp$ production at the ILC is concerned, there are two points of departure: either we will know to some extent what the mass of the charged Higgs boson is or we will not. In the first case it makes sense to combine this knowledge with the knowledge of the cross section prediction in the MSSM and adjust the collider energy to the maximum of the expected cross section as a function of \sqrt{s} . In the second case it is difficult to say what the best strategy of choosing \sqrt{s} will be for searching for the charged Higgs boson. A reasonable assumption is however that a significant fraction of the data during ILC operation will be collected at the highest collider energy.

With these two possibilities in mind, we devised two parameter scans. The first scan assumes that the charged Higgs mass is known and that it makes sense to adjust the collider energy to maximize the cross section. Furthermore, it assumes that one has also acquired some knowledge about the value of $\tan\beta$. We thus fix m_{H^\pm} and $\tan\beta$ in our scan and include \sqrt{s} in the list of scanned parameters. The second scan fixes \sqrt{s} at the maximal collider energy but includes m_{H^\pm} and $\tan\beta$ in the list of scanned parameters. For both scans we assume an ILC with a maximal collision energy of 1 TeV.

In general, we are interested in regions of parameter space where the cross section is large such that it might still be detectable at the ILC. In order to increase the number of scanned parameter points in the region of large cross section, we use the "adaptive scanning" algorithm described in more detail in Ref. [22]. Essentially, that means that we are using the importance sampling algorithm VEGAS [23] to evaluate the integral of the cross section over the relevant MSSM parameters. However, we are not interested in the value of the meaningless integral but store the sampled points which automatically accumulate in the region of large cross section. This method allows to perform scans of

higher-dimensional parameter spaces with emphasis on certain features of the results much more efficiently than a grid of points or purely random sampling can do. More precisely, the quantity we are integrating over in our scans is identical to the cross section only at ‘allowed’ points according to the exclusion limits defined below, and zero otherwise. The enrichment of points thus focuses also on the allowed region. We use the following exclusion limits:

$$\begin{aligned}
m_{\tilde{t}_i} &\geq 95.7 \text{ GeV}, & m_{\tilde{b}_i} &\geq 89 \text{ GeV}, & m_{\tilde{q} \neq \tilde{b}, \tilde{t}} &\geq 150 \text{ GeV}, \\
m_{\tilde{\chi}^0} &\geq 46 \text{ GeV}, & m_{\tilde{\chi}^\pm} &\geq 94 \text{ GeV}, & M_{\tilde{t}} &\geq 73 \text{ GeV}, \\
|\Delta\rho| &\leq 0.0025,
\end{aligned}
\tag{20}$$

where $\Delta\rho$ is the dominant squark contribution to the electroweak rho-parameter. The mass bounds on superpartners and on $\Delta\rho$ are according to Ref. [24].

Apart from these exclusion limits, we take into account two more major constraints on the MSSM parameter space.

Firstly, we calculate for each parameter point the MSSM predictions for m_{h^0} and $\sigma(e^+e^- \rightarrow h^0 Z) \times \text{BR}(h^0 \rightarrow b\bar{b})$ and exclude it if the m_{h^0} -dependent LEP-bound on $\sigma \times \text{BR}$ is violated (according to Table 14(b) of Ref. [25]). We use FeynHiggs 2.5.1 [26] for calculating the m_{h^0} prediction and allow for a theoretical uncertainty of 3 GeV.

Secondly, we calculate the leading-order MSSM prediction for the branching ratio $\text{BR}(B \rightarrow X_s \gamma)$ [27] and exclude parameter points if the prediction falls outside of the range $(3.55 \pm 1.71) \cdot 10^{-4}$. This range is determined by using the experimental central value [28] and adding up the experimental 3σ interval ($\approx 10^{-4}$) and an estimate of the independent theoretical uncertainty ($0.71 \cdot 10^{-4}$). The latter estimate (20%) is guided by the discussion of theoretical uncertainties for the SM prediction [29].

3.3.1 Scan 1: m_{H^\pm} and $\tan\beta$ known

The MSSM input parameters are scanned over the following region:

$$\begin{aligned}
M_{\tilde{f}}, M_1, M_2 &= 10 \dots 2000 \text{ GeV}, \\
\mu, A_t, A_b &= -4000 \dots 4000 \text{ GeV}, \\
\sqrt{s} &= 500 \dots 1000 \text{ GeV}, \\
m_{H^\pm} &= 500 \text{ GeV}, \\
\tan\beta &= 3, 15, 30.
\end{aligned}
\tag{21}$$

The $\tan\beta$ -values respectively lie roughly at the lower, middle, and upper end of the wedge-region. Examining the results by studying projections of the cross section on all one- and two-dimensional subspaces of the scanned parameter space we find that the gaugino mass parameters M_1 and M_2 have negligible influence on the cross section, at least in all regions where the cross section is above 10^{-3} fb. Because of their importance we also study the dependence of the cross section on the squark mixing parameters X_t, X_b normalized to the sfermion mass scale $M_{\tilde{f}}$, i.e. $\hat{X}_t = (A_t - \mu/\tan\beta)/M_{\tilde{f}}$ and $\hat{X}_b = (A_b - \mu\tan\beta)/M_{\tilde{f}}$. In Fig. 8 we show the most interesting two-dimensional projections [30].

For $\tan\beta = 3$ the most noticeable feature, shown in Figs. 8a, 8b and 8c, is that the highest values for the $H^\pm W^\mp$ production cross section lie typically between 10^{-3} fb and 10^{-2} fb and are reached everywhere in the allowed parameter region. In our scan we find a few cases with higher cross section, clearly visible as the scattered yellow dots on a cyan background. Yet, we find no scenario with a cross section above 0.1 fb. The well-known fact that for small $\tan\beta$ the constraints, especially the LEP Higgs-mass bound, require a fair amount of stop mixing (i.e. $|\hat{X}_t| \gtrsim 1$) to be present, is clearly seen in all three figures.

Also owing to the LEP bound, the lowest common squark mass scale $M_{\tilde{f}}$ for which we find allowed scenarios is about 400 GeV for positive \hat{X}_t and 600 GeV for negative \hat{X}_t . It is for rather low $M_{\tilde{f}}$, below about 650 GeV, that the few scenarios with a cross section above 10^{-2} fb appear. It turns out that having $M_{\tilde{f}} \lesssim 650$ GeV is a rather generic necessary requirement for scenarios with cross sections above 10^{-2} fb, as will become more clear in the following.

The projection of the parameter points on the \hat{X}_t - μ plane in Fig. 8c reveals that almost all of the scenarios we find in our scan show a strict correlation between the sign of \hat{X}_t and the sign of μ , the former being positive if the latter is negative and vice versa.

For $\tan\beta = 15$ (Figs. 8d, 8e and 8f) the results of the scan change drastically compared to the $\tan\beta = 3$ case. Firstly, the allowed region in the $M_{\tilde{f}}$ - \hat{X}_t plane (see Fig. 8d) is much larger, now also including scenarios without stop mixing and scenarios with $M_{\tilde{f}}$ below 300 GeV. Secondly, the highest cross section values are considerably larger, of the order of 10 fb. Interestingly, the projection of the parameter points on the $M_{\tilde{f}}$ - \hat{X}_t plane (Fig. 8d) shows that the scenarios with a (large) cross section above 1 fb are confined to a very specific region with $M_{\tilde{f}}$ between 250 GeV and 600 GeV, and \hat{X}_t between -2.5 and -1 simultaneously.

The projection on the \hat{X}_t - \hat{X}_b plane (Fig. 8e) shows that all large cross section scenarios also have a significantly nonzero and negative value of \hat{X}_b . Quantitatively, it turns out that those scenarios typically have the two mass scales $m_t \hat{X}_t$ and $m_b \hat{X}_b$ of the same order of magnitude. Furthermore, from the projection on the \hat{X}_t - μ plane (Fig. 8f) we see that those scenarios also have a positive and large value of μ , typically between 2 TeV and 4 TeV (the limit of our scan range). Looking into the \hat{X}_b - A_b plane (not depicted) we find large cross section scenarios for almost any value of A_b .

The scan results for $\tan\beta = 30$ (Figs. 8g, 8h and 8i) look very similar to the previous case. Again, in order to obtain a cross section above 0.1 fb it appears that one needs a low sfermion mass scale $M_{\tilde{f}}$ between roughly 250 GeV and 600 GeV and a significant amount of mixing in the stop *and* sbottom sector with both \hat{X}_t and \hat{X}_b negative. One important change compared to the previous case is that all large cross section scenarios have a rather large value of $|A_b| \gtrsim 1$ TeV (see Fig. 8i) while the values of μ are constrained to $0.8 \text{ TeV} \lesssim \mu \lesssim 2.2 \text{ TeV}$ (result not depicted).

3.3.2 Scan 2: m_{H^\pm} and $\tan\beta$ unknown

The MSSM input parameters are scanned over the following region:

$$\begin{aligned}
M_{\tilde{f}} &= 10 \dots 2000 \text{ GeV}, \\
\mu, A_t, A_b &= -4000 \dots 4000 \text{ GeV}, \\
m_{H^\pm} &= 500 \dots 920 \text{ GeV}, \\
\tan\beta &= 1 \dots 50, \\
M_1 = M_2 &= 500 \text{ GeV}, \\
\sqrt{s} &= 1 \text{ TeV}.
\end{aligned}
\tag{22}$$

The less influential gaugino-mass parameters M_1, M_2 have been fixed in order to obtain a more thorough scan over the relevant MSSM parameters.

Fig. 9a shows the obtained cross section values projected on the m_{H^\pm} -axis. Overall, the values drop with rising m_{H^\pm} due to decreasing phase space. There are no scenarios with $\sigma > 0.1 \text{ fb}$ for $m_{H^\pm} \gtrsim 750 \text{ GeV}$ and no scenarios with $\sigma > 0.01 \text{ fb}$ for $m_{H^\pm} \gtrsim 875 \text{ GeV}$. The projection on the $\tan\beta$ -axis in Fig. 9b shows that there exist allowed parameter scenarios with cross sections even above 0.1 fb over the whole scanned range. Fig. 9c shows the very distinct dependence of the cross section on the common sfermion mass scale $M_{\tilde{f}}$ which survives even after the inclusion of m_{H^\pm} and $\tan\beta$ in the scan. Evidently, cross sections significantly above 0.1 fb are only possible if $275 \text{ GeV} \lesssim M_{\tilde{f}} \lesssim 700 \text{ GeV}$. A detection of squarks with masses in this range at the LHC would raise hopes that $W^\pm H^\mp$ production would be observable at the ILC with an integrated luminosity of the order of 1000 events/fb.

As in Scan 1 it turns out that the mixing parameters in the third generation squark sector are important for the understanding of the large cross section regions. Fig. 10a shows that the largest cross section values lie roughly on two broad stripes with $1 < |\hat{X}_t| < 2.5$ in the \hat{X}_t - \hat{X}_b plane leaving the central part of the plane with values below 0.01 fb . We find cross section values above 0.1 fb only for scenarios which also have a considerable amount of sbottom mixing, typically $\hat{X}_b \lesssim -50$.

At this point, it is instructive to compare our scan with a variant version where the LEP Higgs constraint on the MSSM parameters is implemented in its most simple way, which is often done in the literature. This simple implementation only makes use of the overall, scenario independent, bound on m_{h^0} (e.g. 89.8 GeV [24]), discarding all scenarios which predict m_{h^0} to lie below it. Obviously, this prescription is overly conservative, keeping e.g. all SM-like scenarios with masses above 89.8 GeV although in this case a bound close to the SM limit of about 114.4 GeV [31] applies.

Fig. 10b shows the results for Scan 2 using the simple implementation of the LEP Higgs constraint. The result looks quite different to the detailed implementation of the constraint in Fig. 10a. The largest cross section values lie roughly scattered around a half-ring in the \hat{X}_t - \hat{X}_b plane. In this less restricted version of Scan 2 a certain amount of squark mixing, either in the stop or sbottom sector is needed in order to obtain cross sections above 0.1 fb .

Motivated by this observation we study the dimensionless quantity

$$\hat{X}_{tb} := \sqrt{\left(\frac{m_t X_t}{M_{\tilde{f}}^2}\right)^2 + \left(\frac{m_b X_b}{M_{\tilde{f}}^2}\right)^2} \quad (23)$$

as a discriminating variable for our original Scan 2. This quantity is just the off-diagonal entries in the stop and sbottom mass matrices, $m_t X_t$ and $m_b X_b$ respectively, added in quadrature and normalized to the common sfermion mass scale $M_{\tilde{f}}$. Fig. 10c shows the projection in the $M_{\tilde{f}}-\hat{X}_{tb}$ plane. Evidently, cross sections above 0.1 fb require $\hat{X}_{tb} \gtrsim 0.8$ and centre roughly around $\hat{X}_{tb} \approx 1$.

4 Conclusions

The production of a charged Higgs boson H^\pm in association with a an electroweak boson W^\mp in e^+e^- collisions is a loop-induced process. At the ILC, this process is particularly important for the charged-Higgs-boson detection if pair production is kinematically forbidden. Furthermore, one would gain valuable information about the underlying model by observing this process at the ILC. We calculated the cross section for this process at one-loop order in the framework of the MSSM and THDM and investigated the predictions of both models at an ILC with 500 GeV and 1000 GeV centre-of-mass energy. The MSSM scenarios with large stop mixing and low sfermion mass scale, for which we showed an example, can give rise to a cross section which differs from a THDM with identical Higgs sector parameters by two orders of magnitude. Using polarized electron and positron beams can increase the cross section by a factor of 2 to 4 depending on m_{H^\pm} and $\tan\beta$. We performed a MSSM parameter scan for regions of large cross section assuming a 1 TeV collider and a charged Higgs boson too heavy to be pair-produced at such a machine. We find scenarios with a cross section above 0.1 fb for m_{H^\pm} up to about 750 GeV in the whole scanned $\tan\beta$ -range (1...50). These scenarios require a sfermion mass scale between 200 GeV and 600 GeV and a certain amount of mixing in the stop and sbottom sector. The FORTRAN program 'eeWH' for the calculation of the MSSM and THDM cross sections including the option to perform parameter scans can be obtained from one of the authors ⁶.

Acknowledgements

We thank Wolfgang Hollik for useful comments. Furthermore, we thank Rachid Benbrik and Sven Heinemeyer for suggesting to improve on the MSSM parameter restrictions we take into account.

⁶Please use the e-mail address oliver.brein@durham.ac.uk

References

- [1] The CMS Collaboration, CMS Technical Design Proposal, CERN/LHCC 94-38; The ATLAS Collaboration, ATLAS Physics Technical Design Report, CERN/LHCC 99-14; The ATLAS and CMS Collaborations, J. G. Branson, D. Denegri, I. Hinchliffe, F. Gianotti, F. E. Paige, P. Sphicas (eds.), hep-ph/0110021; V. Büscher and K. Jakobs, Int. J. Mod. Phys. A **20** (2005) 2523 [hep-ph/0504099].
- [2] J. A. Aguilar-Saavedra et al. [ECFA/DESY LC Physics Working Group Collaboration], hep-ph/0106315; K. Abe et al. [ACFA Linear Collider Working Group], hep-ph/0109166; T. Abe et al. [American Linear Collider Working Group], hep-ex/0106056.
- [3] D. Denegri *et al.*, hep-ph/0112045; K. A. Assamagan, Y. Coadou and A. Deandrea, Eur. Phys. J. direct C **4** (2002) 9 [hep-ph/0203121];
- [4] J. Kalinowski, S. Pokorski, Phys. Lett. B **219** (1989) 116; A. Gutierrez-Rodriguez, O. A. Sampayo, Phys. Rev. D **62** (2000) 055004; A. Gutierrez-Rodriguez, M. A. Hernandez-Ruiz, O. A. Sampayo, Rev. Mex. Fis. **48** (2002) 413 [hep-ph/0110289].
- [5] S. Kanemura, S. Moretti, K. Odagiri, JHEP **0102**, 011 (2001) [hep-ph/0012030].
- [6] A. Djouadi, J. Kalinowski, P. M. Zerwas, Z. Phys. C **54** (1992) 255; B. A. Kniehl, F. Madricardo and M. Steinhauser, Phys. Rev. D **66** (2002) 054016 [hep-ph/0205312]; S. Moretti, Eur. Phys. J. C **34** (2004) 157 [hep-ph/0306297].
- [7] T. Farris, H.E. Logan, S. Su, Phys. Rev. D **69**, 035005 (2004) [hep-ph/0308124].
- [8] O. Brein, T. Hahn, S. Heinemeyer, G. Weiglein, in: *Proceedings of the 10th International Conference On Supersymmetry An Unification Of Fundamental Interactions (SUSY02)*, DESY Hamburg 2002, hep-ph/0402053.
- [9] H.E. Logan, S. Su, Phys. Rev. D **66** (2002) 035001 [hep-ph/0203270]; H.E. Logan, S. Su, Phys. Rev. D **67** (2003) 017703 [hep-ph/0206135].
- [10] S. H. Zhu, hep-ph/9901221.
- [11] S. Kanemura, Eur. Phys. J. C **17** (2000) 473 [hep-ph/9911541].
- [12] A. Arhrib, M. Capdequi Peyranere, W. Hollik, G. Moultaqa, Nucl. Phys. B **581** (2000) 34 [hep-ph/9912527].
- [13] O. Brein, in: *Proceedings of the 10th International Conference On Supersymmetry And Unification Of Fundamental Interactions (SUSY02)*, DESY Hamburg 2002, hep-ph/0209124.

- [14] S. Su, private communication, 2002.
- [15] J.A. Grifols, A. Mendez, Phys. Rev. D **22** (1980) 1725.
- [16] M. Böhm, W. Hollik, H. Spiesberger, Fortsch. Phys. **34** (1986) 687;
P. H. Chankowski, S. Pokorski and J. Rosiek, Nucl. Phys. B **423** (1994) 437
[hep-ph/9303309]; A. Dabelstein, Z. Phys. C **67** (1995) 495 [hep-ph/9409375].
- [17] J. A. Coarasa, D. Garcia, J. Guasch, R. A. Jimenez, J. Sola, Eur. Phys. J. C **2**
(1998) 373 [hep-ph/9607485].
- [18] F. del Aguila, A. Culatti, R. Munoz-Tapia, M. Perez-Victoria, Phys. Lett. B **419**
(1998) 263 [hep-th/9709067]; F. del Aguila and M. Perez-Victoria, Acta Phys. Polon.
B **28** (1997) 2279 [hep-ph/9710442].
- [19] J. Küblbeck, M. Böhm, A. Denner, Comput. Phys. Commun. **60** (1990) 165;
H. Eck, Ph.D. thesis, University of Würzburg (1995);
T. Hahn and M. Perez-Victoria, Comput. Phys. Commun. **118** (1999) 153
[hep-ph/9807565];
T. Hahn, Comput. Phys. Commun. **140** (2001) 418 [hep-ph/0012260];
T. Hahn and C. Schappacher, Comput. Phys. Commun. **143** (2002) 54
[hep-ph/0105349].
- [20] S. Heinemeyer, W. Hollik and G. Weiglein, Eur. Phys. J. C **9** (1999) 343
[hep-ph/9812472].
- [21] O. Brein, W. Hollik, Eur. Phys. J. C **13** (2000) 175 [hep-ph/9908529]; O. Brein,
W. Hollik and S. Kanemura, Phys. Rev. D **63** (2001) 095001 [hep-ph/0008308].
- [22] O. Brein, Comput. Phys. Commun. **170** (2005) 42 [hep-ph/0407340].
- [23] G. P. Lepage, J. Comput. Phys. **27** (1978) 192; G. P. Lepage, Report CLNS-80/447
(Cornell University, LNS).
- [24] S. Eidelman et al. [Particle Data Group Collaboration], Phys. Lett. B **592** (2004) 1.
- [25] S. Schael *et al.* [ALEPH Collaboration], Eur. Phys. J. C **47**, 547 (2006).
- [26] S. Heinemeyer, W. Hollik and G. Weiglein, Eur. Phys. J. C **9** (1999) 343 and
Comput. Phys. Commun. **124**, 76 (2000);
G. Degrossi, S. Heinemeyer, W. Hollik, P. Slavich and G. Weiglein, Eur. Phys. J. C
28 (2003) 133;
M. Frank, T. Hahn, S. Heinemeyer, W. Hollik, H. Rzehak and G. Weiglein,
hep-ph/0611326.

- [27] A. L. Kagan and M. Neubert, Phys. Rev. D **58** (1998) 094012 and Eur. Phys. J. C **7** (1999) 5;
The code we are using is taken from T. Hahn, W. Hollik, J. I. Illana and S. Peñaranda, hep-ph/0512315.
- [28] S. Chen *et al.* [CLEO Collaboration], Phys. Rev. Lett. **87** (2001) 251807;
B. Aubert *et al.* [BABAR Collaboration], hep-ex/0207074;
E. Barberio *et al.* [Heavy Flavor Averaging Group (HFAG)], hep-ex/0603003.
- [29] M. Misiak *et al.*, Phys. Rev. Lett. **98** (2007) 022002.
- [30] The complete results of the parameter scans can be obtained via the following URL:
<http://www.ippp.dur.ac.uk/~obr/eeWH-scan/>.
- [31] R. Barate *et al.* [LEP Working Group for Higgs boson searches], Phys. Lett. B **565** (2003) 61.

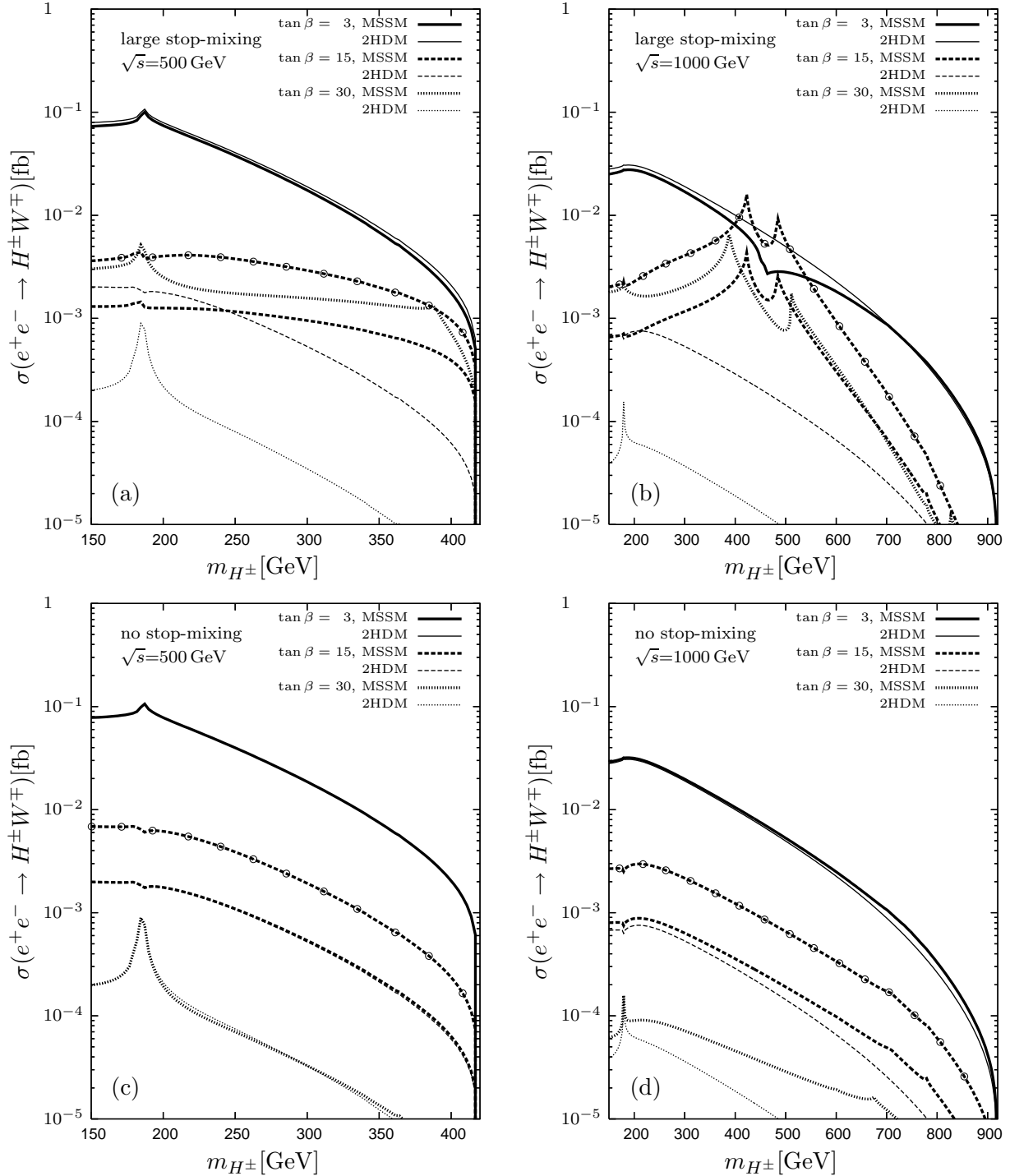


Figure 5: Cross section $\sigma(e^+e^- \rightarrow H^\pm W^\mp)$ versus m_{H^\pm} for different values of $\tan\beta$. MSSM predictions of the large-stop-mixing and no-stop-mixing scenarios for the unpolarized cross section are displayed (thick lines) along with the corresponding sTHDM scenario (thin lines) for a collider energy of $\sqrt{s} = 500$ GeV and $\sqrt{s} = 1000$ GeV. The cross section for optimal polarization, $P(e^-) = -1$ and $P(e^+) = +1$, is shown for the case $\tan\beta = 15$ (thick lines with circles).

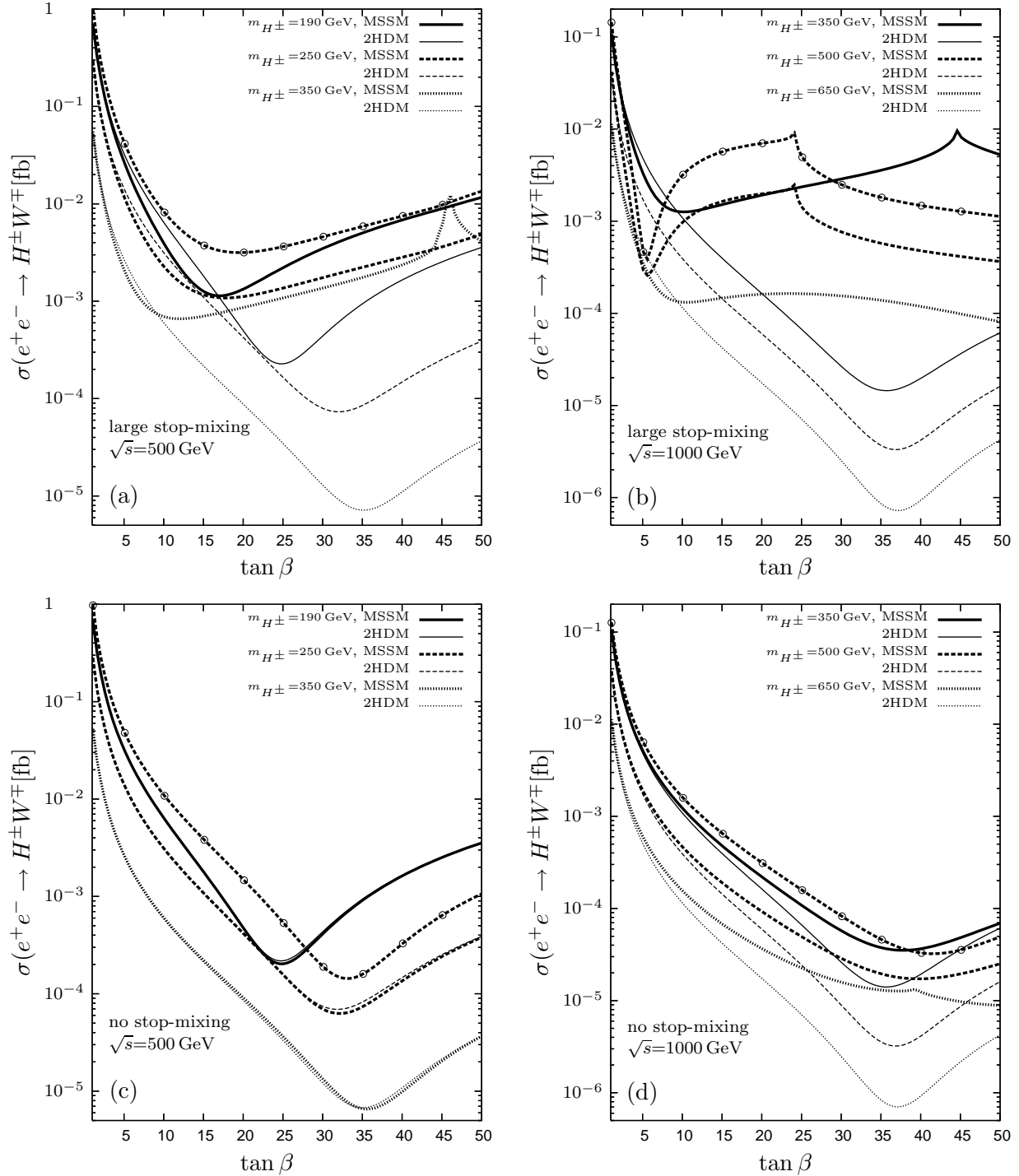


Figure 6: Cross section $\sigma(e^+e^- \rightarrow H^\pm W^\mp)$ versus $\tan \beta$ for different values of m_{H^\pm} . MSSM predictions of the large-stop-mixing and no-stop-mixing scenarios for the unpolarized cross section are displayed (thick lines) along with the corresponding sTHDM scenario (thin lines) for a collider energy of $\sqrt{s} = 500$ GeV and $\sqrt{s} = 1000$ GeV. The cross section for optimal polarization, $P(e^-) = -1$ and $P(e^+) = +1$, is shown in each panel for the case $m_{H^\pm} = \sqrt{s}/2$ (thick lines with circles).

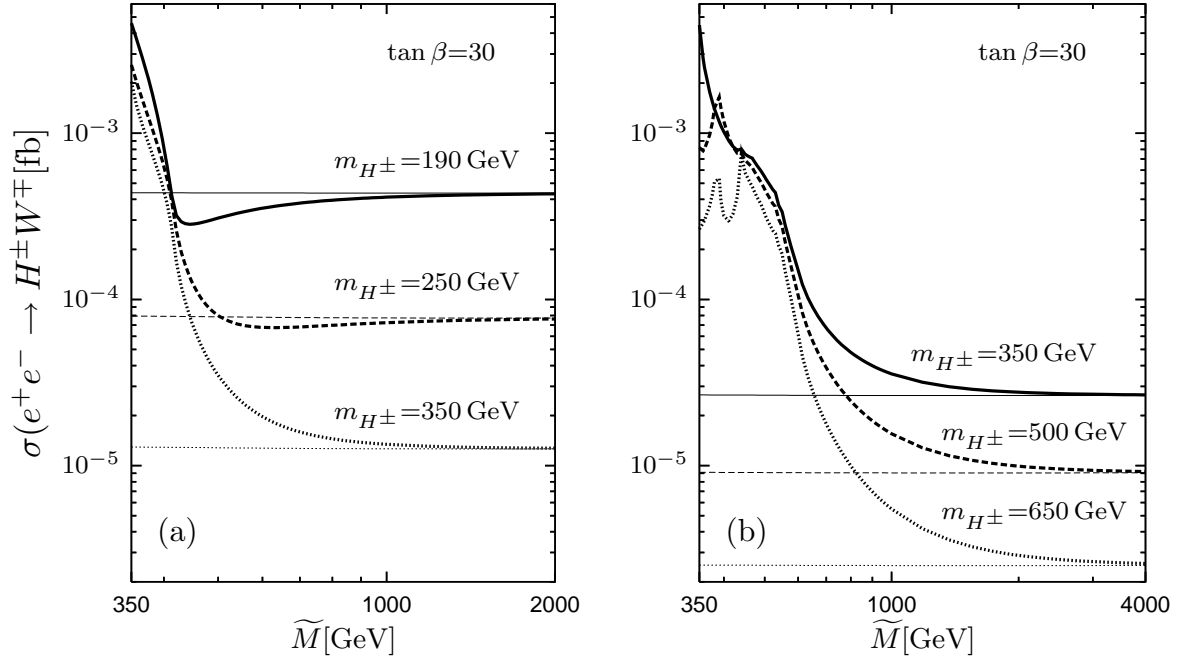


Figure 7: Cross section for the process $e^+e^- \rightarrow H^\pm W^\mp$ as a function of a common superpartner mass scale \tilde{M} for a (a) 500 GeV and (b) 1 TeV e^+e^- collider.

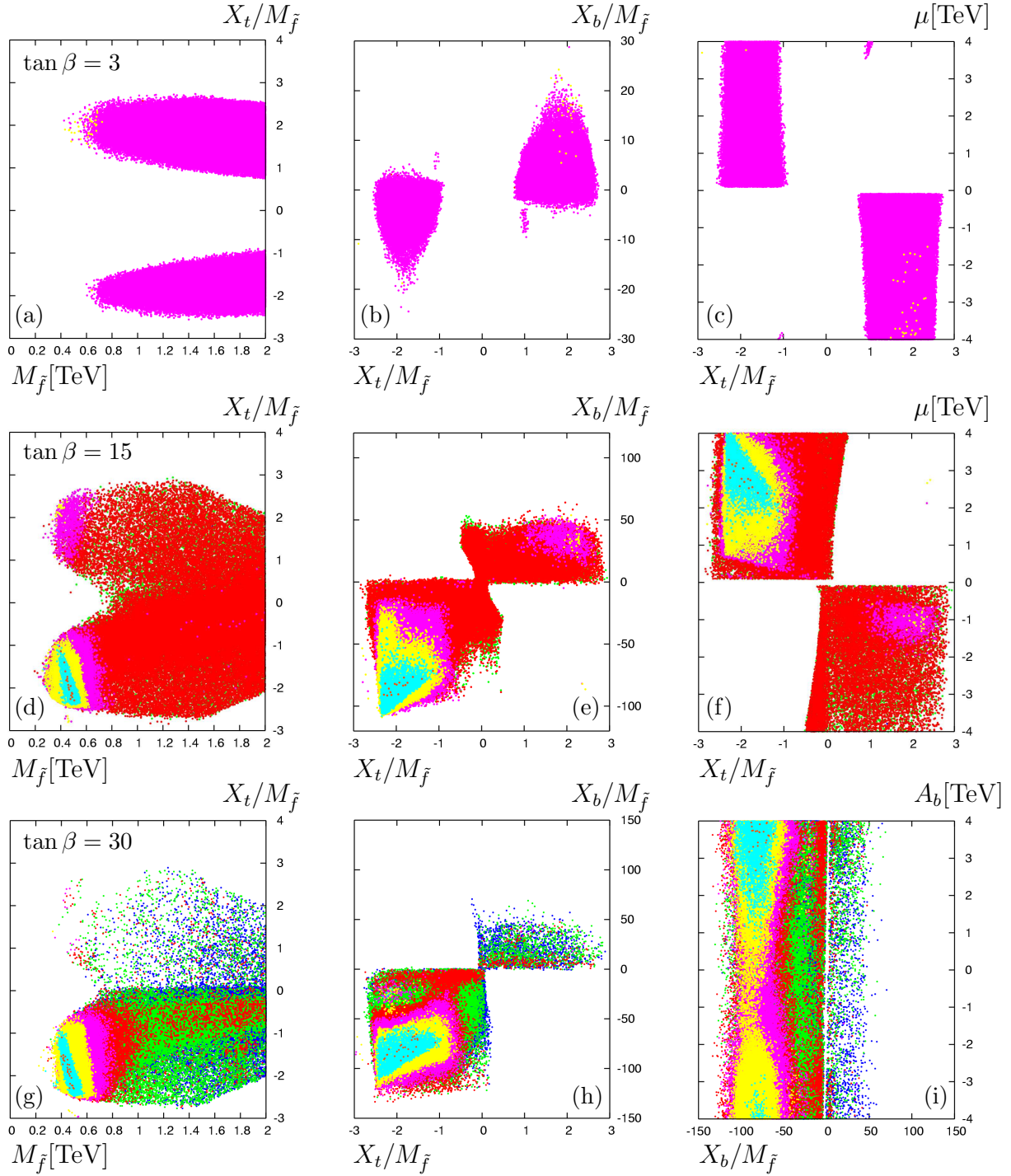


Figure 8: Two dimensional slices through the scanned parameter space of Scan 1 for $\tan \beta = 3, 15$ and 30 . The colours refer to bins of cross section values: **orange**: $10\text{fb} \geq \sigma > 1\text{fb}$, **light blue**: $1\text{fb} \geq \sigma > 10^{-1}\text{fb}$, **yellow**: $10^{-1}\text{fb} \geq \sigma > 10^{-2}\text{fb}$, **cyan**: $10^{-2}\text{fb} \geq \sigma > 10^{-3}\text{fb}$, **red**: $10^{-3}\text{fb} \geq \sigma > 10^{-4}\text{fb}$, **green**: $10^{-4}\text{fb} \geq \sigma > 10^{-5}\text{fb}$, **blue**: $\sigma < 10^{-5}\text{fb}$. Points with larger values of σ are plotted on top of points with smaller values.

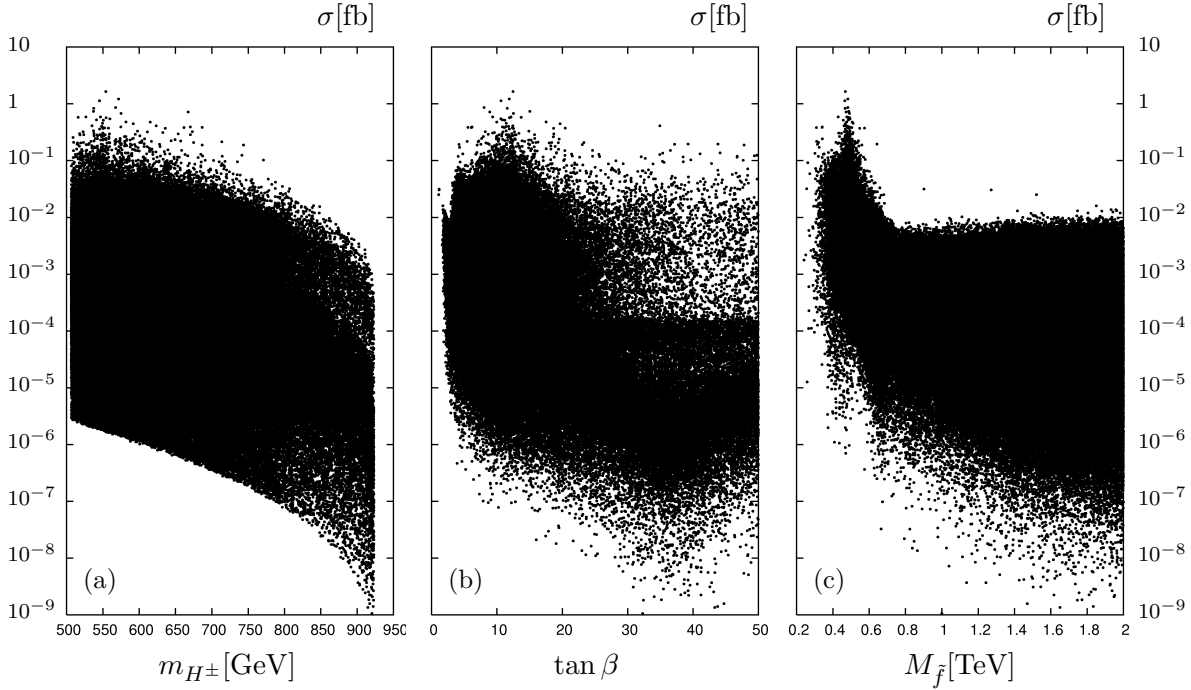


Figure 9: Cross section results of Scan 2 versus (a) m_{H^\pm} , (b) $\tan \beta$ and (c) $M_{\tilde{f}}$.

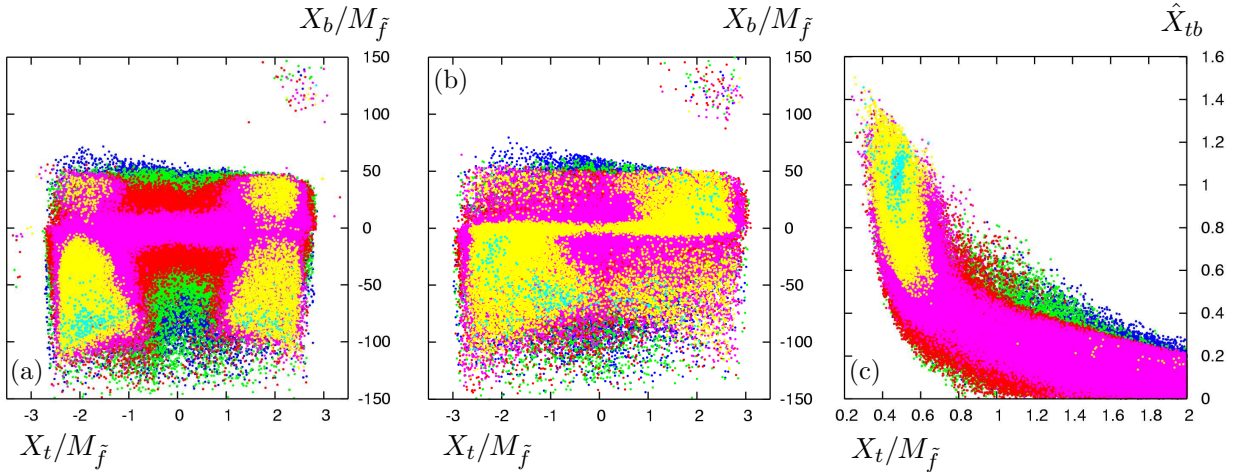


Figure 10: Two dimensional slices through the scanned parameter space of Scan 2. The middle panel (b) shows the same slice as panel (a) but for a variant of Scan 2 which uses a simple implementation of the LEP constraint (see text). The quantity \hat{X}_{tb} in panel (c) is defined in Eq. (23). The colours refer to bins of cross section values in the same way as in Fig. 8. Points with larger values of σ are plotted on top of points with smaller values.